High temperature thermoelectric properties of the type-I clathrate Ba8NixGe46-x-y y

Umut Aydemir, Christophe Candolfi, Alim Ormeci, Michael Baitinger, Niels Oeschler, Franck Steglich, Yuri Grin

High temperature thermoelectric properties of the type-I clathrate $Ba_8Ni_xGe_{46-x-y}\square_y$

U. Aydemir,[1,2] C. Candolfi,[1,+] A. Ormeci,[1] M. Baitinger,[1] N. Oeschler,[1] F. Steglich,[1]

Yu. Grin[1,*]

[1] *Max-Planck-Institut für Chemische Physik fester Stoffe, Nöthnitzer Str. 40, 01187 Dresden, Germany*

[2] *Koç University, Rumelifeneri Yolu, Sarıyer, Istanbul 34450, Turkey*

[*] Corresponding author: Juri.Grin@cpfs.mpg.de

+ Present address: Institut Jean Lamour, UMR 7198 CNRS – Université de Lorraine, Parc de Saurupt, CS 50840, 54011 Nancy, France

Abstract

Polycrystalline samples of the type-I clathrate $Ba_8Ni_xGe_{46-x-y}\square_y$ were synthesized for $0.2 \leq x \leq 3.5$ by melt quenching and for $3.5 < x \leq 6.0$ by melting with subsequent annealing at 700 °C. The maximum Ni content in the clathrate framework at this temperature was found to be $x \approx 4.2$ atoms per unit cell. Thermoelectric and thermodynamic properties of the type-I clathrate were investigated from 300 to 700 K by means of electrical resistivity, thermopower, thermal conductivity and specific heat measurements. As the Ni content increases, the electronic properties gradually evolve from a metallic character ($x < 3.5$) towards a highly-doped semiconducting state ($x \geq 3.5$). Below $x \approx 4.0$ transport is dominated by electrons, while further addition of Ni ($x \approx 4.2$) switches the electrical conduction to *p*-type. Maximum values of the dimensionless thermoelectric figure of merit $ZT \approx 0.2$ were achieved at 500 K and 650 K for $x \approx 2.0$ and $x \approx 3.8$, respectively.

I. Introduction

The thermoelectric properties of a material are described by the dimensionless thermoelectric figure of merit defined as $ZT = \alpha^2 T / \rho\kappa$.[1,2] High ZT values require achieving simultaneously a large thermopower α, low electrical resistivity ρ and low thermal conductivity κ. Many state-of-the-art thermoelectric materials are optimized to behave as heavily doped semiconductors, which exhibit the most favorable combination of the three properties above.[3]

Type-I clathrates have emerged as a class of prospective materials for thermoelectric applications at high temperatures.[4,5] With the general formula $G'_2G''_6X_{46}$ (G', G'' represent alkali metals, alkaline-earth metals and Eu; X stands for Al, Ga, Si, Ge, Sn as well as transition metals or vacancy), clathrates usually crystallize in the cubic space group $Pm\bar{3}n$ (No. 223). The framework is built upon four-bonded X atoms comprising two pentagonal dodecahedra (12 pentagonal faces; 5^{12}) and six tetrakaidecahedra (12 pentagonal and 2 hexagonal faces; $5^{12}6^2$) per unit cell (Figure 1). The G' and G'' atoms are encapsulated in the pentagonal dodecahedra and the tetrakaidecahedra, respectively.

In designing semiconducting clathrates, the Zintl formalism can be applied to predict the chemical composition at which, the n-to-p-type transition occurs. In this concept, electropositive atoms donate their valence electrons to the more electronegative part of the structure to form covalent bonds and satisfy the valence requirements in the anionic part (8-N Pearson rule).[20] When fulfilled, this concept roughly reflects the carrier concentration of the material, which is crucial in optimizing the thermoelectric performance. Among the variety of type-I clathrate phases existing so far, the ternary compounds $Ba_8M_xGe_{46-x-y}\square_y$ (M = Ga, Zn, Cu, Al, Ni, Pd, Pt, etc.) stand for the most promising candidates for high-temperature thermoelectric applications,[6-18] since in these cases, semiconducting behavior can be achieved

at a suitable chemical composition. An increasing amount of systematic studies is currently devoted to the impact of the *M* atoms on the crystal structure as well as on the electronic and phononic transport properties. These studies are essential in clarifying which kind of substitution element *M* may lead to a substantial improvement in the thermoelectric performance. Prominent examples with high *ZT* values are $Ba_8Ni_{0.31}Zn_{0.52}Ga_{13.06}Ge_{32.2}$ (*ZT* of ≈ 1.2 at 1000 K) and in $Ba_8Au_{5.3}Ge_{40.7}$ (*ZT* of ≈ 0.9 at 1000 K).[14,21] These results have demonstrated that substitution of framework elements is a fruitful strategy to optimize the thermoelectric performance of type-I clathrates by reducing the lattice thermal conductivity. In the system Ba – Ni – Ge, the thermoelectric properties at low temperatures were reported for different clathrate-I compositions,[22-24] but a systematic exploration of the high temperature range is still missing. The thermoelectric properties of Bridgman-grown single crystals of $Ba_8Ni_{3.5}Ge_{42.1}\square_{0.4}$ at low and high temperatures were recently investigated.[6]

Continuing our studies of several type-I clathrate phases, we investigate here the high-temperature thermoelectric properties of the polycrystalline clathrate phase $Ba_8Ni_xGe_{46-x-y}\square_y$ in the Ni concentration range ($0 \leq x \leq 4.2$) representing the whole homogeneity range. The objectives of this study are manifold: to examine whether the description of transport using Boltzmann transport theory can be extended above room temperature, to improve our understanding of the relationship between Ni (*x*) and vacancy (*y*) contents and the thermal transport via a detailed analysis of the specific heat and the lattice thermal conductivity, and to assess the potential of this phase for thermoelectric applications in its temperature range of interest.

II. Experimental details

Polycrystalline samples of $Ba_8Ni_xGe_{46-x-y}\square_y$ with nominal compositions $0 \leq x \leq 6.0$ (Table I) were prepared from Ba pieces (ChemPur, 99.9 %), Ni powders (ChemPur, 99.99 %) and Ge pieces (ChemPur, 99.9999 %). As a first step, stoichiometric amounts of the elements were placed in glassy carbon crucibles and melted using an induction furnace inside an Ar-filled glove box. Subsequently, the melt was quenched between two cold stainless steel plates. After melting, the samples with higher Ni content ($3.5 < x \leq 4.2$) were annealed at 700 °C for 4 days. For the annealing process, the ingots were placed in glassy carbon crucibles sealed in tantalum tubes and jacketed in quartz ampoules. After annealing, the ampoules were quenched in water.

Structural and chemical characterizations were carried out by using powder X-ray diffraction (PXRD), energy dispersive X-ray spectroscopy (EDXS) and wavelength dispersive X-ray spectroscopy (WDXS). PXRD data were collected at room temperature using an X-ray Guinier diffraction technique (Huber G670 camera, Cu-$K\alpha_1$ radiation, $5° \leq 2\theta \leq 100°$). The reflection positions were determined by profile deconvolution and corrected using LaB_6 (a = 4.15683 Å) as internal standard. The lattice parameters of clathrate compounds were calculated from least-square refinements with the WinCSD program package.[25] Microstructure analysis of polished bulk samples was carried out by using a Philips XL 30 SEM with integrated EDX spectrometer. The chemical compositions of the clathrate phase were determined with WDXS (Cameca SX 100, tungsten cathode) using Ba_6Ge_{25} and Ni as external standards. Hereafter, the nominal compositions will be used to label the samples.

Thermopower and electrical resistivity were simultaneously measured from 300 to 650 K with a commercial setup (ZEM-3, UlvacRiko) on bar-shaped specimens, cut with a diamond-wire saw from the ingots into typical dimensions of $2\times2\times6$ mm^3. For all samples, densities

were found to be about 95% of the theoretical densities. Hall effect measurements were performed with the ac transport option of a physical property measurement system (PPMS, Quantum Design) at 300 K. Prism-shaped specimens ($6\times6\times1$ mm^3) were cut to measure, between 300 and 650 K, the thermal diffusivity a which is related to the thermal conductivity κ via $\kappa = aC_p\rho_V$, where C_p is the specific heat and ρ_V is the volume mass. The thermal diffusivity and specific heat were measured by a laser flash (LFA 427, Netzsch) and a differential scanning calorimetric techniques (Pegasus, Netzsch), respectively. The value of the linear thermal expansion coefficient $\alpha_T \sim 12.25\times10^{-6}$ K^{-1} at 300 K, measured on a $Ba_8Ni_{5.8}Ge_{40.2}$ sample by Johnsen *et al.*[22] was used to evaluate $\rho_V(T)$. As a first approximation, the value of α_T was considered to be temperature- and composition-independent.

III. Results and discussion

A. Characterization of the samples

Samples with compositions $x \leq 3.5$ were obtained either as single-phase ones, or with minor admixtures of the neighboring phases (Table I, Figure 2). The low fraction of secondary phases observed in the present samples should affect minimally the transport properties measured, which can be thus considered as the intrinsic properties of the type-I clathrates. The sample with the nominal composition $x = 6.0$ contained larger amounts of NiGe and $BaGe_2$ as by-products which contrasts with prior results suggesting the existence of compositions between $x = 4.0$ and $x = 6.0$.[22] From the dependence of the lattice parameter with x, the solubility limit was found at $x = 4.2$. For $x \leq 1.0$, X-ray powder diffraction patterns of the clathrate phase showed a $2a\times2a\times2a$ supercell. Analogously to the binary $Ba_8Ge_{43}\square_3$ (space

group $Ia\bar{3}d$), it can be assumed that the supercell formation at low Ni contents results from an ordered arrangement of sites partially occupied in space group $Pm\bar{3}n$. All samples with larger Ni concentration do not show the superstructure reflections in PXRD patterns, so the clathrate-I phase is described with the *a*×*a*×*a* subcell and space group $Pm\bar{3}n$.

B. Thermopower and electrical resistivity

Figure 3 shows the temperature dependence of the thermopower for the samples studied. A transition from an electron-dominated transport to hole transport is observed on going from *x* = 4.0 to *x* = 4.2. Of note, the Ni concentration at which the crossover occurs is lower than that reported by Johnsen *et al.*[22] (*x* = 5.8) and by Xu *et al.*[23] (*x* = 4.9). In the latter report, this value was estimated from the *x*-dependence of the carrier concentration measured in samples of nominal compositions *x* = 3.0, *x* = 4.0 and *x* = 6.0. Yet, since only the nominal compositions were reported, the *x* = 6.0 sample may show an actual Ni content lower than the nominal one according to our results (see Table I) leading to an overestimation of the Ni concentration delineating the two regimes. Below *x* = 3.0, $|\alpha|$ increases linearly with temperature up to 650 K, indicative of a dominating diffusion thermopower. In this concentration range, the variations in the $|\alpha|$ values depend on the Ni content. It can be thus concluded that incorporation of Ni atoms in the framework causes a decrease in the electron concentration, leading to an increase in $|\alpha|$. Above *x* = 3.0 and up to *x* = 4.0, a clear departure from linearity emerges. $|\alpha|$ first increases, shows a maximum and then decreases with temperature. The maximum in $|\alpha|(T)$ is shifted towards lower temperatures as the Ni content increases. From the peak thermopower $\alpha_{\max}$, an estimation of the thermal band gap can be obtained using $E_g = 2e\alpha_{\max}T_{\max}$ where e is the elementary charge and $T_{\max}$ is the temperature at which the maximum is reached. This

yields band gaps of 150, 166, 148 and 144 meV for the x = 3.5, 3.8, 4.0 and 4.2 samples, respectively. The slight variation with the Ni content suggests that a rigid-band evolution of the electronic band structure may not be fully appropriate in the present case.

The overall evolution of $\alpha(T)$ is consistent with a progressive loss of degeneracy as x increases resulting from a shift of the Fermi level towards the conduction band edge. This is clearly seen in the carrier concentration that decreases with increasing x (Table II). We note that the carrier concentration measured by Xu *et al.*[23] slightly deviate from the present values. Given the rapid decrease in n between x = 2.0 and x = 3.5 (see Table II), variations in the Ni content between their samples and ours may explain these differences. The Ni content therefore enables controlling the electronic properties and driving the system from a nearly-compensated semi-metallic state (x = 0) towards a highly-doped semiconducting state for $x \geq 3.5$.[7,15] The x = 4.2 sample does not represent an exception to this behavior, the maximum being already reached near 300 K. Thus, the high-temperature data of this sample reflect the influence of minority carriers.

When the Fermi level approaches the band edge, a more quantitative analysis of the thermopower requires the Fermi-Dirac statistics while simplifications of these integrals are usually sufficient to describe transport in the degenerate regime *i.e.* in the metallic state. The degeneracy of the system can be further examined by considering the so-called Ioffe-Pisarenko curves which represent the carrier-concentration dependence of $\alpha(T)$ at a given temperature.[1,2] For degenerate semiconductors, $|\alpha|$ is expected to increase linearly with temperature T and to follow a $n^{-2/3}$ dependence[26]

$$|\alpha| = -\frac{8\pi^2 k_B^2 m^*}{3eh^2} T \left(\frac{\pi}{3n}\right)^{\frac{2}{3}} (1+\lambda) \qquad (1)$$

where k_B is the Boltzmann constant, m^* is the effective mass of the charge carriers, e (< 0) is the elementary charge, h is the Planck constant and λ is a scattering constant related to the energy dependence of the electronic scattering rate. Figure 4 shows the $|\alpha|$ values measured at 400 and 500 K plotted versus the carrier concentration supposed to be constant in the temperature range studied. Here, we restrict our analysis to the *n*-type samples ($2.0 \leq x \leq 4.0$) and to these temperatures to avoid the influence of minority carriers on transport. The experimental data are compared to theoretical curves calculated using Eq.(1) and using the solution of the Boltzmann transport equation in the relaxation-time approximation[26]

$$|\alpha| = -\frac{k_B}{e}\left(\frac{(2+\lambda)F_{1+\lambda}(\eta)}{(1+\lambda)F_{\lambda}(\eta)} - \eta\right) \tag{2}$$

$$n = \frac{4}{\sqrt{\pi}}\left(\frac{2\pi m^* k_B T}{h^2}\right)^{\frac{3}{2}} F_{\frac{1}{2}}(\eta) \tag{3}$$

where η is the reduced chemical potential and $F_i(\eta)$ is the Fermi integral of order *i*. In both calculations, we assumed that neutral-impurity scattering, which is the main scattering mechanism near 300 K, still dominates at these temperatures so that $\lambda = 1/2$.[7] The values of the electron concentration (or hole concentration for the x = 4.2 sample) used in these calculations were inferred from results of measurements of the Hall effect at 300 K.[7] In Eq.(1), we used a constant effective mass m^* of $3.5\,m_0$ (m_0 is the bare electron mass) while in Eq.(3), a slightly higher value ($m^* = 4.5\,m_0$) was utilized. As shown in Figure 4, the experimental data are well described by the degenerate limit (Eq.(1)) for $n \geq 1.6 \times 10^{21}$ cm^{-3}. At lower electron concentrations, a clear departure from this limit appears. These results are consistent with the analysis carried out at 300 K revealing that the Fermi-Dirac statistics should be used to describe transport in the highly-doped semiconducting regime ($x \geq 3.5$).[7] These conclusions therefore

still hold above 300 K and at least up to 500 K. The m^* values, however, show a slight variation as a function of both concentration and temperature. This indicates that the assumptions of a constant effective mass and/or a single parabolic band may not be fully applicable in the present system. Hence, it is no surprise that a change in m^* appears, which suggests that the details of the electronic band structure (*e.g.* the width of the band gap and curvature of the bands) vary with *x*, specifically on approaching $x = 4.0$.[7]

Figure 5 shows the high-temperature electrical resistivity data. At low Ni content ($x < 2.0$), ρ decreases with increasing temperature mimicking a semiconducting behavior. These dependences contrast with those observed at low temperature, indicating a typical metallic-like behaviour.[7] In $Ba_8Ge_{43}\square_3$, this seeming metal-insulator transition was shown to be due to multiband conduction.[15] The simultaneous presence of both types of carriers appears to extend over a large window of Ni concentrations (up to $x = 2.0$), thereby explaining the behavior of ρ. At higher Ni contents ($x = 3.0$), a metallic-like behavior is recovered. A decrease of the $\rho(T)$ values occurs above 600 K for the $x = 3.5$, 3.8 and 4.0 samples and likely reflects the contribution of minority carriers as already seen in the thermopower data. The $x = 4.2$ sample displays a semiconducting behavior typified by a decrease of $\rho(T)$ in the whole temperature range and consistent with the high thermopower values measured.

C. Specific heat and thermal conductivity

An accurate assessment of the thermal conductivity at high temperatures necessitates determining the temperature dependence of the specific heat C_p. In the absence of high-temperature data, the Dulong-Petit law is usually used to approximate C_p. However, this approach reflects the lattice vibrations of a harmonic crystal and does not take into account the

anharmonicity, which increases with temperature owing to the thermal expansion of the unit cell. This last feature, usually referred to as the quasi-harmonic term, gives an additional contribution to C_p which then exceeds the Dulong-Petit value ($C_v = 3k_B / atom$ *i.e.* 1272 and 1347 $J\ mol^{-1}\ K^{-1}$ for x = 0.0 and 4.0, respectively).[27] Figure 6 shows the $C_p(T)$ data collected on samples with x = 0.0 up to x = 4.2. Regardless of the Ni content, the C_p values exceed the Dulong-Petit limit above room temperature and rise linearly with temperature following the thermal expansion of the unit cell. However, both the temperature at which the $C_p(T)$ data crosses the Dulong-Petit limit and the slope of the linear variation depends on the Ni content. Both characteristics evolve with x, the former increasing with the Ni content (from 260 K for x = 0.2 up to 360 K for x = 4.2) while the latter decreases concomitantly (from 0.507 $J\ mol^{-1}\ K^{-2}$ for x = 0.2 to 0.371 $J\ mol^{-1}\ K^{-2}$ for x = 4.2). These variations suggest that the vacancies and their ordering have little influence on $C_p(T)$ at high temperatures. To unveil a possible anharmonic contribution beyond the quasi-harmonic approximation, associated with the temperature dependence of phonons at a constant volume, a separation of the phononic and the electronic contributions would be required. This last term is related to the first temperature derivative of the electron entropy, which represents the availability of unoccupied states above the Fermi level and may be calculated from first-principles calculations. This electronic contribution can be significant in metals at high temperatures since it is expected to linearly increase with temperature as long as the charge carriers remain degenerate. The assumption of degenerate charge carriers is however no longer valid for the samples with $3.5 < x \leq 4.2$ as revealed by the $\alpha(T)$ data. This and the fact that the progressive addition of Ni lowers the electronic contribution suggest that this term might also play a role in the variation of the slope with x.

The $C_p(T)$ data were modeled by a linear function and extrapolated up to 700 K to derive

the temperature dependence of the thermal conductivity shown in Figure 7. Below x = 3.0, κ slightly increases with temperature. Above this Ni content, the κ values remain constant before increasing with temperature at 550 K for x = 3.5 and at 450 K for x = 3.8, 4.0 and 4.2. These temperatures match those where the thermopower shows an extremum clearly indicating the thermal activation of minority carriers. This feature yields an additional contribution to the thermal conductivity, the so-called bipolar contribution, which results in a steep rise in the thermal conduction. The thermal conductivity shows a broad range of values that decrease with increasing the Ni content. Much of this variation may be due to the variations in the electrical resistivity of the samples. To confirm this hypothesis, the thermal conductivity can be divided into three contributions so that κ can be described as a sum of electronic, lattice and bipolar terms:

$$\kappa = \kappa_e + \kappa_L + \kappa_{bipolar} \tag{4}$$

For a metal, the electronic contribution κ_e is usually estimated via the Wiedemann-Franz law $\kappa_e = L_0 T / \rho$ with $L_0 = 2.44 \times 10^{-8}\ V^2 K^{-2}$. However, the shift of the Fermi level towards the conduction band edges results in a loss of degeneracy, which lowers the Lorenz number $L(T) = \kappa_e(T)$. In principle, L depends on the scattering mechanism, on temperature and on the majority and minority carrier concentrations making the determination of L a nontrivial task. A good estimation of this parameter can nevertheless be obtained using the above-mentioned parabolic single-band model. In this description, the Lorenz number can be expressed as[26]

$$L = \frac{k_B^2}{e^2} \frac{(1+\lambda)(3+\lambda)F_\lambda(\eta)F_{2+\lambda}(\eta) - (2+\lambda)^2 F_{1+\lambda}(\eta)^2}{(1+\lambda)^2 F_\lambda(\eta)^2} \tag{5}$$

The values of L, listed in Table III, were estimated at room temperature for all the samples using the η values derived from the $\alpha(T)$ data by Eq.(2). As expected, L varies only slightly with *x* up to *x* = 3.0 while a clear departure from L_0 occurs when *x* approaches *x* = 4.0. The separation of the electronic term from the lattice and the bipolar contributions was achieved assuming a temperature-independent value of L for $x \leq 3.0$ while for the *x* = 3.5 and *x* = 3.8 samples, the temperature dependence was taken into account by calculating L at several temperatures. In the case of the *x* = 4.0 and *x* = 4.2 samples, this model breaks down due to the strong influence of minority carriers. Yet, the electronic contribution is significantly lower because of the large ρ values and only amounts to 5.8 and 1.9% at 300 K, respectively. The $\kappa(T)$ data therefore mainly reflect the lattice contribution and can be directly compared to the other data.

Figures 8a, 8b and 8c show κ_L and κ_e as a function of temperature, respectively. Note that because of the influence of minority carriers effect, which is not taken into account in Eq.(5), the data presented for the *x* = 3.5 and *x* = 3.8 samples are restricted to the 300 – 500 K temperature range. Furthermore, we did not attempt to estimate the bipolar contribution so that the data shown in Figure 8b corresponds to $\kappa_L + \kappa_{Bipolar}$. Regardless of the Ni concentration, the κ_L values vary between 1.5 and 3.0 W m^{-1} K^{-1} at 300 K. The addition of Ni tends to decrease κ_L, the lowest values being achieved in the *x* = 0.8, *x* = 4.0 and *x* = 4.2 samples. At first sight, it appears surprising that a Ni content as low as 0.8 is sufficient to strongly lower κ_L as higher Ni concentrations do. This result might be ascribed to the ordered crystal structure (similar to that of the binary $Ba_8Ge_{43}\square_3$) which seems to remain unaffected with increasing *x* up to *x* = 1.0. Another possibility could be related to the hybridization between the phonon modes of the Ba atoms and the acoustic phonons of the Ge-Ni framework, as recently observed by inelastic neutron scattering experiments carried out on single crystalline $Ba_8Ni_{3.5}Ge_{42.1}\square_{0.4}$.[28] This

coupling results in an anti-crossing behavior of the phonon dispersion curves that disrupts efficiently the propagation of the heat-carrying acoustic phonons thereby lowering the thermal transport. The observed *x*-dependence confirms the low-temperature data, which revealed a marked decrease in the magnitude of the low-temperature peak for $0 < x \leq 1.0$.[7] The $x = 4.0$ and $x = 4.2$ samples show very similar κ_L values indicating a minimal influence of the *n*-*p* type transition at high temperatures. This situation thus contrasts with the picture seen at low temperatures where crossing the *n*-*p* type border drives the disappearance of the dielectric maximum in the *p*-type sample. Though not fully elucidated, the larger effective mass of holes in the $x = 4.2$ sample with respect to the *n*-type samples (see Table III) might play an important role in this disappearance via an increased hole-phonon scattering.

D. Thermoelectric figure of merit ZT

From the combination of the $\rho(T)$, $\alpha(T)$ and $\kappa(T)$ data, the dimensionless figure of merit *ZT* was calculated and is shown in Figure 9 as a function of temperature. Maximum *ZT* values of 0.2 at 500 and 650 K are achieved for the $x = 2.0$ and $x = 3.8$ samples, respectively. The observed decrease at high temperatures originates from minority carrier effects, which affect adversely both the thermopower and the thermal conductivity. It is interesting to notice that the maximum *ZT* is also reached in the $x = 2.0$ sample *i.e.* in a composition off the compositional range where a highly-doped semiconducting state is observed.

IV. Conclusion

We reported on the thermoelectric properties of the clathrate-I phase $Ba_8Ni_xGe_{46-x-y}\square_y$ in the homogeneity range extending from $x = 0$ up to $x = 4.2$. The electronic properties

progressively evolve towards a semiconducting state with increasing x. Crossing the x = 4.0 concentration, the conduction switches from n- to p-type. On a more quantitative level, the variations in the electronic properties with the carrier concentration were described over a broad temperature range by simple theoretical models. The maximum ZT value of around 0.2 for x = 2.0 and 3.8 for $Ba_8Ni_xGe_{46-x-y}\square_y$ remains lower than that of the best Ge-based and Ba-containing type-I clathrates.

Acknowledgment

The authors thank Petra Scheppan, Renate Hempel-Weber and members of the Kompetenzgruppe Struktur for providing experimental support. C.C. acknowledges the financial support of the CNRS-MPG program. Yu.G. gratefully acknowledges financial support by the Deutsche Forschungsgemeinschaft (SPP 1386).

References

[1] H.J. Goldsmid in *Thermoelectric Refrigeration* (Temple Press Books Ltd, London, 1964).

[2] Thermoelectrics and its Energy Harvesting, edited by D. M. Rowe (CRC Press, 2012).

[3] G. J. Snyder and E. S. Toberer, Nature Mater. **7**, 114 (2008).

[4] M. Christensen, S. Johnsen and B. B. Iversen, Dalton Trans. **39**, 978 (2010).

[5] K. A. Kovnir and A. V. Shevelkov, Russ. Chem. Rev. **73**, 923 (2004).

[6] L. T. K. Nguyen, U. Aydemir, M. Baitinger, E. Bauer, H. Borrmann, U. Burkhardt, J. Custers, A. Haghighirad, R. Höfler, K. D. Luther, F. Ritter, W. Assmus, Yu. Grin and S. Paschen, Dalton Trans. **39**, 1071 (2010).

[7] U. Aydemir, C. Candolfi, A. Ormeci, M. Baitinger, N. Oeschler, F. Steglich and Yu. Grin, to be published.

[8] Ya. Mudryk, P. Rogl, C. Paul, S. Berger, E. Bauer, G. Hilscher, C. Godart and H. Noël, J. Phys.: Condens. Matter **14**, 7991 (2002).

[9] E. Alleno, G. Maillet, O. Rouleau, E. Leroy, C. Godart, W. Carrillo-Cabrera, P. Simon and Yu. Grin, Chem. Mater. **21**, 1485 (2009).

[10] S. Y. Rodriguez, L. Saribaev and J. R. Ross Jr, Phys. Rev. B **82**, 064111 (2010).

[11] N. Melnychenko-Koblyuk, A. Grytsiv, P. Rogl, H. Schmid, G. Giester, J. Solid State Chem. 182, 1754 (2009).

[12] N. Melnychenko-Koblyuk, A. Grytsiv, P. Rogl, M. Rotter, E. Bauer, G. Durand, H. Kaldarar, R. Lackner, H. Michor, E. Royanian, M. M. Koza and G. Giester, Phys. Rev. B **76**, 144118 (2007).

[13] N. Melnychenko-Koblyuk, A. Grytsiv, P. Rogl, M. Rotter, R. Lackner, E. Bauer, L. fornasari, F. Marabelli and G. Giester, Phys. Rev. B **76**, 195124 (2007).

[14] X. Shi, J. Yang, S. Bai, J. Yang, H. Wang, M. Chi, J. R. Salvador, W. Zhang, L. Chen and

W. Wong-Ng, Adv. Funct. Mater. **20**, 755 (2010).

[15] C. Candolfi, U. Aydemir, M. Baitinger, N. Oeschler, Yu. Grin and F. Steglich, Phys. Rev. B **84**, 205118 (2011).

[16] C. Candolfi, U. Aydemir, M. Baitinger, N. Oeschler, F. Steglich and Yu. Grin, J. Electron. Mater. **39**, 2039 (2010).

[17] U. Aydemir, C. Candolfi, H. Borrmann, M. Baitinger, A. Ormeci, W. Carrillo-Cabrera, C. Chubilleau, B. Lenoir, A. Dauscher, N. Oeschler, F. Steglich and Yu. Grin, Dalton Trans. **39**, 1078 (2010).

[18] A. F. May, E. S. Toberer, A. Saramat and G. J. Snyder, Phys. Rev. B **80**, 125205 (2009).

[19] J. Martin, H. Wang and G. S. Nolas, Appl. Phys. Lett. **92**, 222110 (2008).

[20] H. Schäfer, B. Eisenman and W. Müller, Angew. Chem. Int. Ed. **12**, 694 (1973).

[21] H. Zhang, H. Borrmann, N. Oeschler, C. Candolfi, W. Schnelle, M. Schmidt, U. Burkhardt, M. Baitinger, J.-T. Zhao and Yu. Grin, Inorg. Chem. **50**, 1250 (2011).

[22] S. Johnsen, A. Bentien, G. K. Madsen, M. Nygren and B. B. Iversen, Phys. Rev. B **76**, 245126 (2007).

[23] J. Xu, J. Wu, S. Heguri, G. Mu, Y. Tanabe and K. Tanigaki, J. Elec. Mater. **41**, 1177 (2012); J. Xu, J. Wu, Y. Tanabe, S. Heguri, G. Mu, H. Shimatori, K. Tanigaki, J. Elec. Mater. **41**, 2025 (2012).

[24] W. Wong-Ng, Q. Huang, I. Levin, J. C. Woicik, X. Shi, J. Yang and J. A. Kaduk, Powder Diff. **27**, 25 (2012).

[25] L. G. Akselrud, Yu. Grin, J. Appl. Cryst. **47**, 803 (2014).

[26] V. I. Fistul, *Heavily Doped Semiconductors* (Plenum Press, New York, 1969).

[27] B. Fultz, Prog. Mater. Sci. **55**, 247 (2010).

[28] H. Euchner, S. Pailhès, L. T. K. Nguyen, W. Assmus, F. Ritter, A. Haghighirad, Yu. Grin, S. Paschen, M. de Boissieu, Phys. Rev. B **86**, 224303 (2012).

Tables

Table I. Nominal, measured compositions (WDXS), observed phases (C-I stands for the clathrate-I phase) and lattice parameters (a) of $Ba_8Ni_xGe_{46-x-y}\square_y$. For each sample, the amount of by-products estimated from XRPD is also given.

Nominal composition	*WDXS composition*	*Observed phases*	*a* (Å)
$Ba_8Ge_{43}\square_3$	$Ba_{8.00(1)}Ge_{42.99(4)}$	C-I (100 mass%)	21.3079(2) (a/2 = 10.6540)
$Ba_8Ni_{0.2}Ge_{42.8}$	$Ba_{8.00(2)}Ni_{0.19(2)}Ge_{42.89(3)}$	C-I (> 97 mass%) + α-Ge (< 3 mass%)	21.3085(3) (a/2 = 10.6543)
$Ba_8Ni_{0.5}Ge_{42.5}$	$Ba_{8.0(1)}Ni_{0.6(2)}Ge_{42.7(2)}$	C-I (> 99 mass%) + α-Ge (< 1 mass%)	21.3140(2) (a/2 = 10.6570)
$Ba_8Ni_{0.8}Ge_{42.2}$	$Ba_{8.0(1)}Ni_{0.9(2)}Ge_{42.5(2)}$	C-I (> 99 mass%) + α-Ge (< 1 mass%)	21.3151(2) (a/2 = 10.6576)
$Ba_8Ni_{1.0}Ge_{42.0}$	$Ba_{8.0(1)}Ni_{1.0(2)}Ge_{43.1(3)}$	C-I (> 97 mass%) + Ba_6Ge_{25} (< 3 mass%)	21.3166(2) (a/2 = 10.6583)
$Ba_8Ni_{2.0}Ge_{42.0}$	$Ba_{8.0(1)}Ni_{2.1(2)}Ge_{43.0(3)}$	C-I (> 99 mass%) + Ba_6Ge_{25} (< 1 mass%)	10.6678(1)
$Ba_8Ni_{3.0}Ge_{42.0}$	$Ba_{8.00(3)}Ni_{3.07(2)}Ge_{42.45(3)}$	C-I (100 mass%)	10.6788(1)
$Ba_8Ni_{3.5}Ge_{42.0}$	$Ba_{8.00(2)}Ni_{3.49(5)}Ge_{42.34(5)}$	C-I (100 mass%)	10.6803(1)
$Ba_8Ni_{3.8}Ge_{42.0}$	$Ba_{8.00(3)}Ni_{3.90(1)}Ge_{42.03(4)}$	C-I (> 97 mass%) + α-Ge (< 3 mass%)	10.6787(1)
$Ba_8Ni_{4.0}Ge_{42.0}$	$Ba_{8.0(1)}Ni_{4.0(2)}Ge_{42.0(1)}$	C-I (> 99 mass%) + α-Ge (< 1 mass%)	10.6780(1)
$Ba_8Ni_{4.2}Ge_{41.8}$	$Ba_{8.00(3)}Ni_{4.08(1)}Ge_{41.87(3)}$	C-I (> 99 mass%) + α-Ge (< 1 mass%)	10.6771(1)
$Ba_8Ni_{6.0}Ge_{40}$	$Ba_{8.00(2)}Ni_{4.22(1)}Ge_{41.29(7)}$	C-I (> 90 mass%) + α-Ge (< 6 mass%) + $BaGe_2$ (< 4 mass%)	10.6765(1)

Table II. Room temperature values of the electron (n) and hole (p) concentrations, Seebeck coefficient (α), electrical resistivity (ρ), total thermal conductivity (κ) and lattice (κ_L) and electronic (κ_e) thermal conductivity of $Ba_8Ni_xGe_{46-x-y}\square_y$. n and p were obtained via Hall effect measurements presented in detail in Ref. 7. For compositions $x \leq 1.0$, the presence of both holes and electrons do not allow a direct estimation of each carrier concentration. Note that, at 300 K, the bipolar contribution to the thermal conductivity is not present so that Eq.(4) reduces to $\kappa = \kappa_e + \kappa_L$.

Nominal composition (x)	n (p) (10^{21} cm^{-3})	α (μV K^{-1})	ρ (μΩ m)	κ (W m^{-1} K^{-1})	κ_e (W m^{-1} K^{-1})	κ_L (W m^{-1} K^{-1})
0.0	/	1.6	16.6	4.5	0.44	4.06
0.2	/	-1.0	10.7	2.7	0.68	2.02
0.5	/	-4.5	7.0	2.3	1.04	1.26
0.8	/	-9.8	10.8	2.6	0.67	1.93
1.0	/	-11.4	8.9	2.5	0.82	1.68
2.0	6.1	-25.5	11.1	2.2	0.65	1.55
3.0	3.6	-38.5	19.4	1.9	0.37	1.53
3.5	1.6	-67.2	7.7	2.3	0.88	1.42
3.8	0.26	-152.0	56.6	1.9	0.11	1.79
4.0	0.19	-172.0	64.1	1.9	0.09	1.80
4.2	0.75	215.0	102.7	1.5	0.06	1.44

Table III. Effective masses (m^*/m_0) and Lorenz number (L) calculated at 300 K using equations (2), (3) and (5).

Nominal composition (x)	*m*/m₀*	L ($\times 10^{-8}$ $V^2.K^{-2}$)
2.0	2.8	2.42
3.0	3.1	2.38
3.5	3.1	2.28
3.8	3.6	2.03
4.0	2.5	1.99
4.2	9.0	1.94

Figure Captions

Figure 1: Crystal structure of the type-I clathrate $Ba_8Ni_xGe_{46-x-y}\square_y$. The framework atoms are located at the 6*c* (white), 16*i* (grey) and 24*k* (red) sites while the guest atoms Ba′ and Ba″ are located at the 2*a* and 6*d* (orange) sites, respectively. The Ni atoms and the vacancies are mainly observed at the 6*c* site. The pentagonal dodecahedra and the tetrakaidecahedra are shown in blue and green, respectively.

Figure 2: PXRD patterns (Cu-$K\alpha_1$) of $Ba_8Ni_xGe_{46-x-y}\square_y$ samples with nominal compositions x = 0.5, 3.5, and 6.0. The lower and upper ticks mark the positions of primitive cell reflections ($Ba_8Ni_{3.5}Ge_{42.1}\square_{0.4}$ [Ref. 6]) as well as additional superstructure reflections, respectively. The most intense reflections of the observed by-products are also marked.

Figure 3: Temperature dependence of the thermopower of $Ba_8Ni_xGe_{46-x-y}\square_y$ for (a) x = 0 (○), x = 0.2 (□), x = 0.5 (◊), x = 0.8 (△), x = 1.0 (●), x = 2.0 (+) and x = 3.0 (▼) and (b) for x = 3.5 (♦), x = 3.8 (■), x = 4.0 (▲) and x = 4.2 (▼).

Figure 4: Carrier concentration dependence of the thermopower (in absolute values) measured at 400 (●) and 500 K (■) of the x = 2.0, 3.0, 3.5, 3.8 and 4.0 samples (cf. Table II). The experimental data are compared to the degenerate limit (black dotted curve obtained from Eq.(1)) and to a single-parabolic band model using the Fermi-Dirac statistics (black solid lines calculated from Eq.(2) and Eq.(3)).

Figure 5: Temperature dependence of the electrical resistivity of $Ba_8Ni_xGe_{46-x-y}\square_y$ (a) for $x = 0$ (○), $x = 0.2$ (□), $x = 0.5$ (◊), $x = 0.8$ (Δ), $x = 1.0$ (●), $x = 2.0$ (+), $x = 3.0$ (▼) and (b) for $x = 3.5$ (♦), $x = 3.8$ (■), $x = 4.0$ (▲) and $x = 4.2$ (▼).

Figure 6: (a) Specific heat C_p of $Ba_8Ni_xGe_{46-x-y}\square_y$ as a function of temperature for $x = 0$ (○), $x = 0.2$ (□), $x = 0.5$ (◊), $x = 0.8$ (Δ), $x = 1.0$ (●), $x = 2.0$ (+), $x = 3.0$ (▼), $x = 3.5$ (♦) and $x = 4.2$ (▼) samples. (b) $C_p - C_v$ versus temperature for the same samples.

Figure 7: Temperature dependence of the thermal conductivity of $Ba_8Ni_xGe_{46-x-y}\square_y$ for (a) $x = 0$ (○), $x = 0.2$ (□), $x = 0.5$ (◊), $x = 0.8$ (Δ), $x = 1.0$ (●), $x = 2.0$ (+) and $x = 3.0$ (▼) and (b) for $x = 3.5$ (♦), $x = 3.8$ (■), $x = 4.0$ (▲) and $x = 4.2$ (▼).

Figure 8: Temperature dependence of the lattice thermal conductivity of $Ba_8Ni_xGe_{46-x-y}\square_y$ for (a) $x = 0$ (○), $x = 0.2$ (□), $x = 0.5$ (◊), $x = 0.8$ (Δ), $x = 1.0$ (●), $x = 2.0$ (+) and $x = 3.0$ (▼) samples and (b) for $x = 3.5$ (♦), $x = 3.8$ (■), $x = 4.0$ (▲) and $x = 4.2$ (▼). The bipolar contribution that shows up in samples with high Ni contents ($x \geq 3.5$) has not been subtracted. At low Ni contents ($x < 3.5$), this contribution is negligible. (c) Electronic thermal conductivity versus temperature for the same samples (except for $x = 4.0$ and $x = 4.2$). Note that for the $x = 3.5$ and $x = 3.8$ samples, the data were only extracted up to 500 K *i.e.* where minority carriers have no influence on the thermal transport.

Figure 9: Temperature dependence of the dimensionless thermoelectric figure of merit *ZT* of $Ba_8Ni_xGe_{46-x-y}\square_y$ for $x = 0.2$ (□), $x = 0.5$ (◊), $x = 0.8$ (Δ), $x = 1.0$ (●), $x = 2.0$ (+), $x = 3.0$ (▼), $x = 3.5$ (♦), $x = 3.8$ (■), $x = 4.0$ (▲) and $x = 4.2$ (▼).

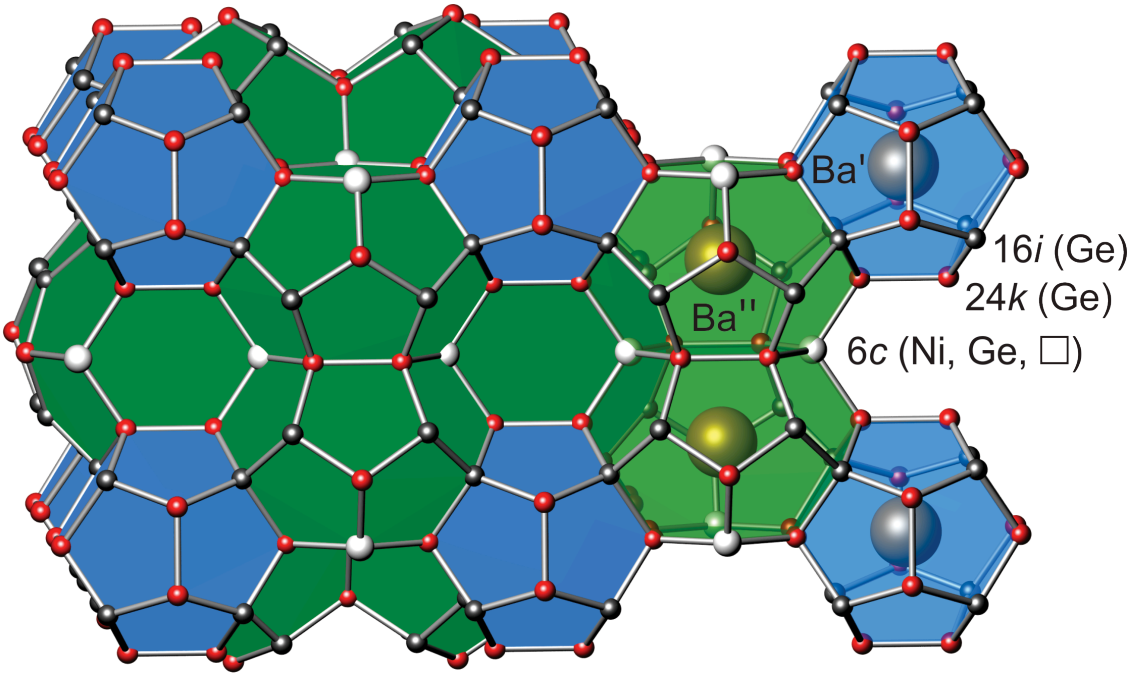

Figure 1

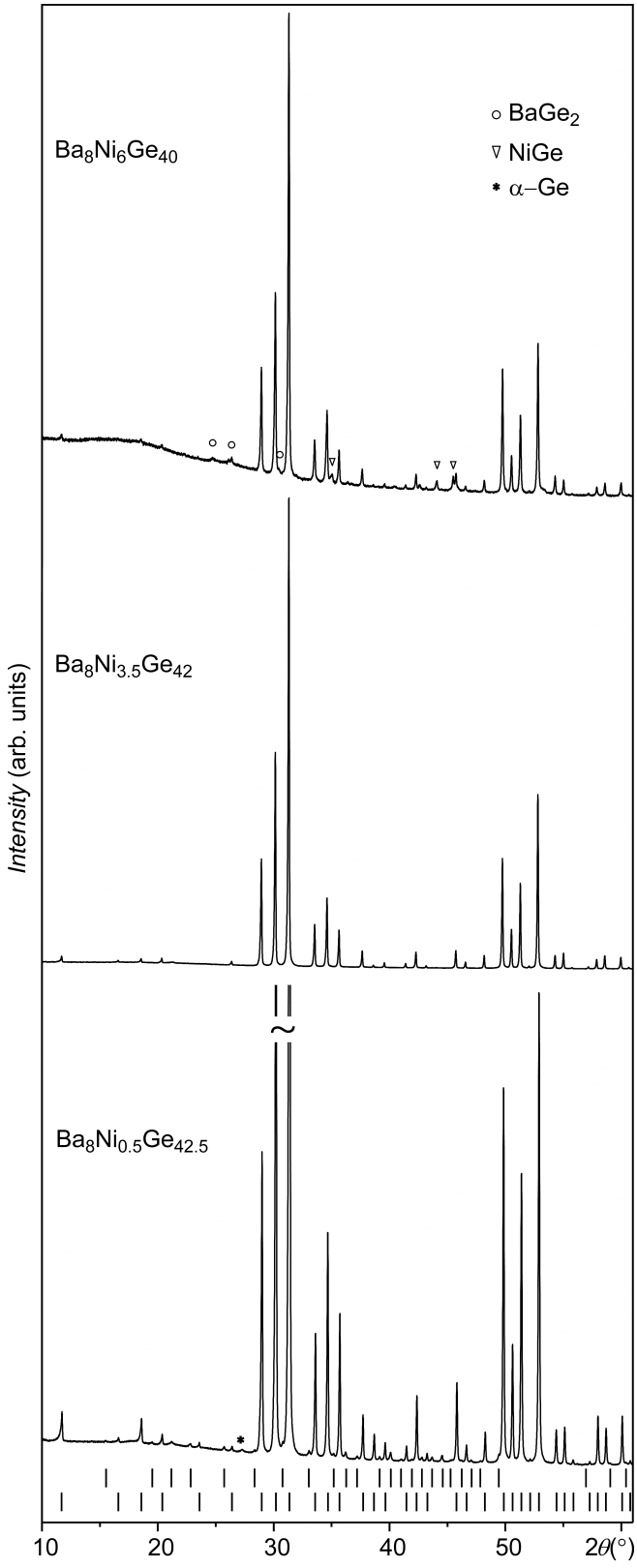
Ba8Ni6Ge40
○ BaGe2
▽ NiGe
* α–Ge
Ba8Ni3.5Ge42
Ba8Ni0.5Ge42.5
Intensity (arb. units)
10
20
30
40
50
2θ(°)

Figure 2

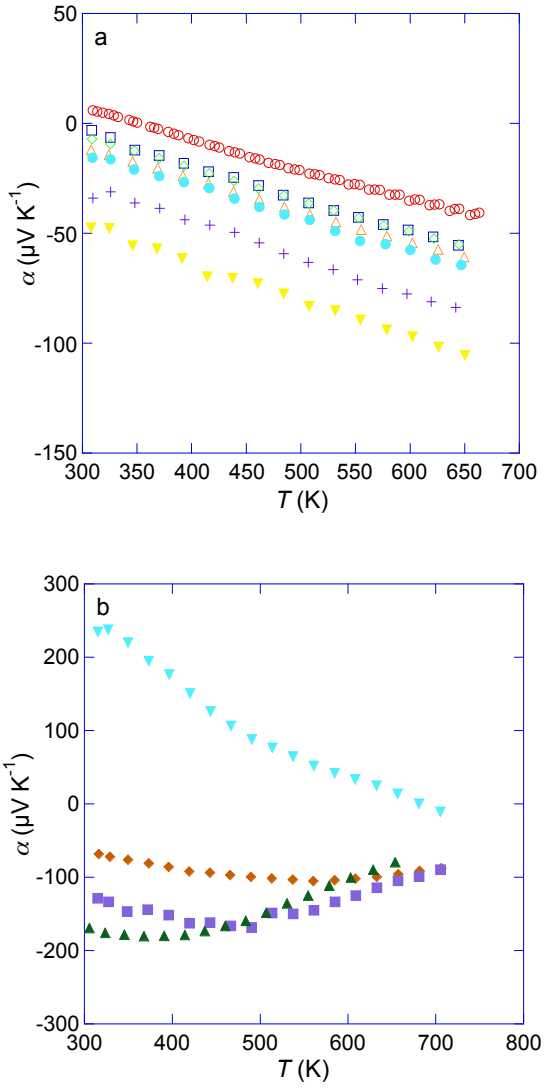
a
50
0
-50
-100
-150
300 350 400 450 500 550 600 650 700
T (K)
α (μV K-1)
b
300
200
100
0
-100
-200
-300
300 400 500 600 700 800
T (K)
α (μV K-1)

Figure 3

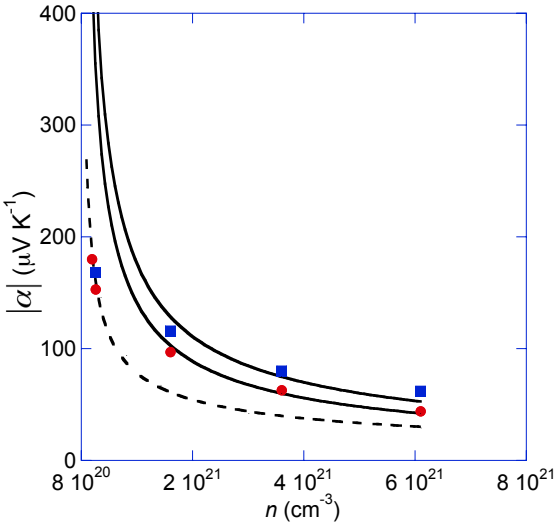

Figure 4

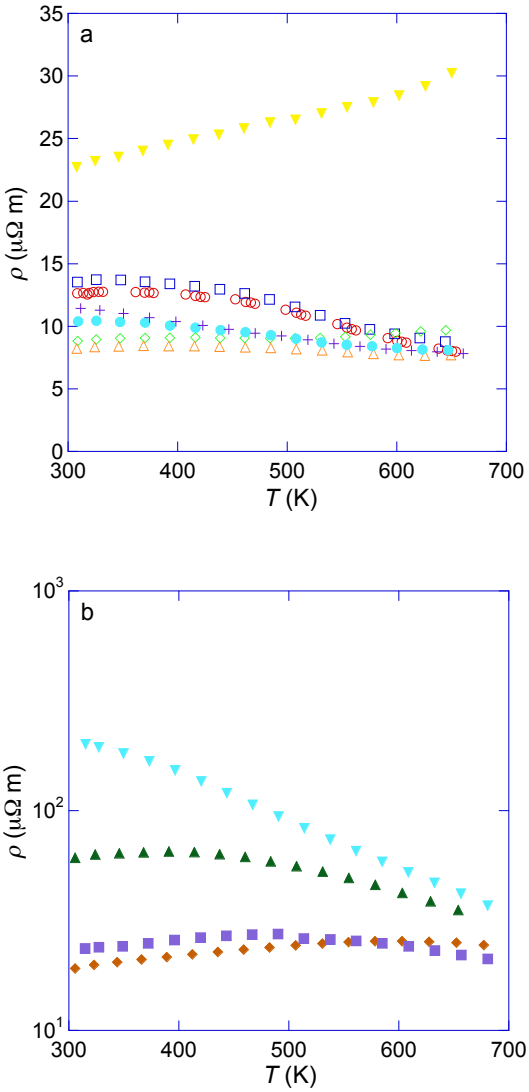
a
35
30
25
20
15
10
5
0
300
400
500
600
700
T (K)
ρ (μΩ m)
b
10^3
10^2
10^1
300
400
500
600
700
T (K)
ρ (μΩ m)

Figure 5

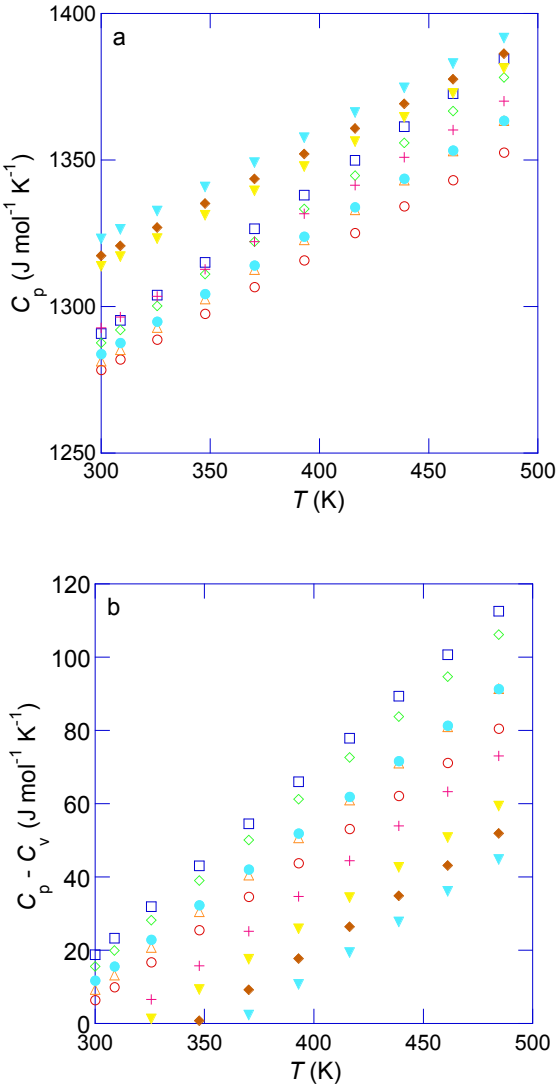
a
1400
1350
1300
1250
300
350
400
450
500
C_p (J mol^{-1} K^{-1})
T (K)
b
120
100
80
60
40
20
0
300
350
400
450
500
C_p - C_v (J mol^{-1} K^{-1})
T (K)

Figure 6

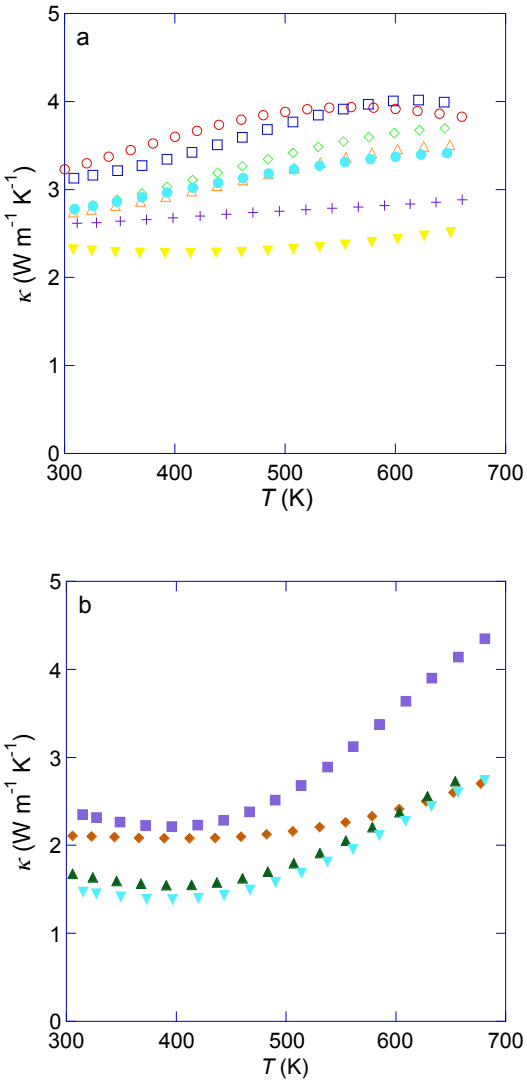

Figure 7

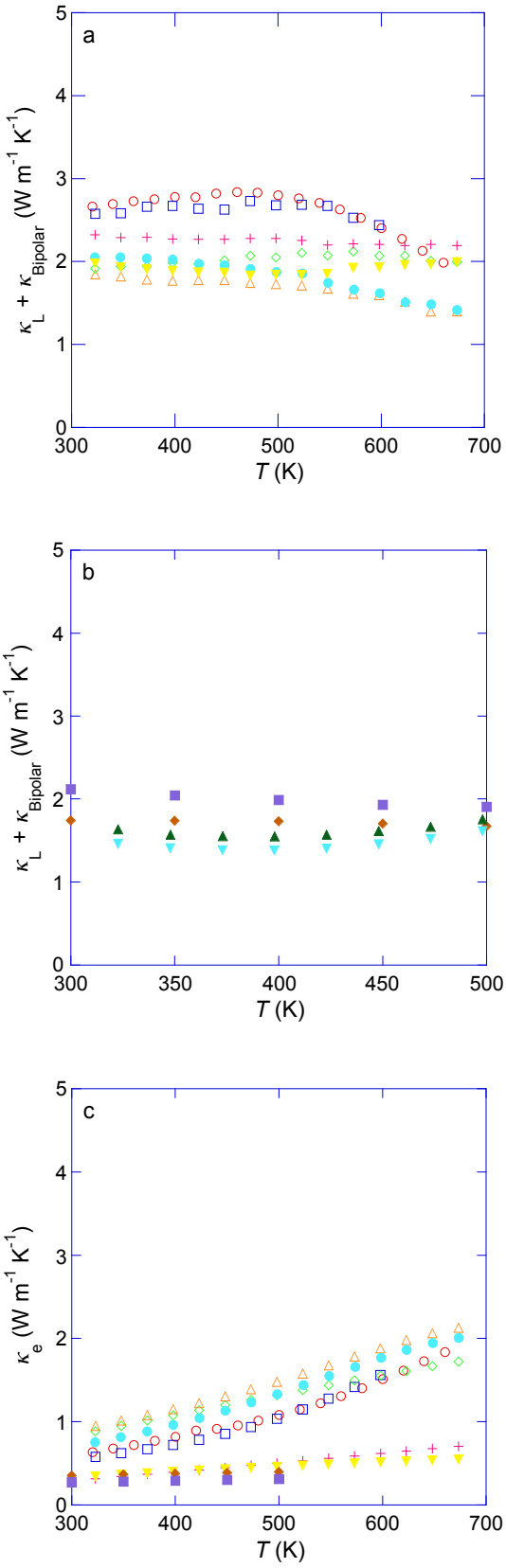

Figure 8

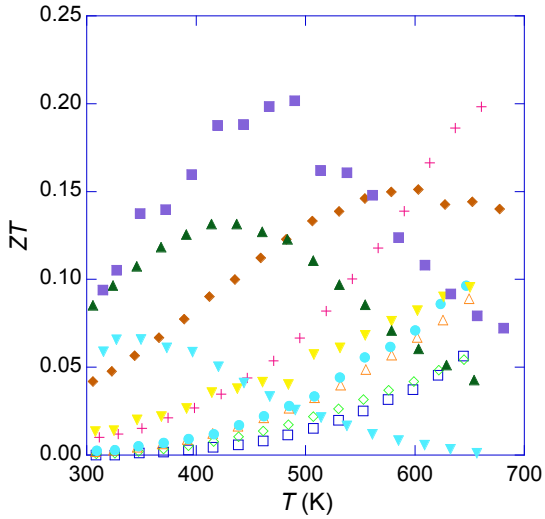

Figure 9